



Attachment mode performance of network-modeled ballistic fabric shielding

D.A. Powell^{a,*}, T.I. Zohdi^b

^aStanford University, 496 Lomita Mall, Stanford, CA 94305-4035, USA

^bDepartment of Mechanical Engineering, 6195 Etcheverry Hall, University of California, Berkeley, CA 94720-1740, USA

ARTICLE INFO

Article history:

Received 9 December 2008

Accepted 30 January 2009

Available online 7 May 2009

Keywords:

A. Ballistics

A. Fabrics/textiles

B. Stress concentrations

C. Computational modelling

ABSTRACT

A central issue in the use of ballistic fabric shielding is the mode of attachment to the structure that it is intended to protect. In order to investigate this issue, a discrete multi-scale yarn-network model is developed for structural fabric undergoing ballistic impact, based on work found in Zohdi and Powell [Zohdi TI, Powell D. Multiscale construction and large-scale simulation of structural fabric undergoing ballistic impact. *Comput Meth Appl Mech Eng* 2006;195:94–109] and Zohdi [Zohdi TI. Modeling/simulation of progressive penetration of multilayered ballistic fabric shielding. *Comput Mech* 2002;29:61–7]. The model is comprised of a network of yarn with stochastic properties determined by smaller-scale fibrils, which are randomly misaligned. The effects of stochasticity on the overall response are explored, and the model is compared against macro-scale experiments. The key feature of the model is the fact that it does not depend on phenomenological parameters, and can be calibrated by simply measuring the properties of an individual, smallest-scale, fibril. The properties of a fibril are easily ascertained from a simple tension test. The response of the overall fabric model and ballistic experiments are in excellent agreement. The model indicates that fabric which is attached by being pinned at the corners generally absorbs more energy, relative to fabric clamped along the sides. The basis for this result is discussed at length in the body of this work. Furthermore, it is observed that a uniform-yarn model, one which ignores the stochastic nature of the yarn, over-estimates the amount of energy absorbed.

© 2009 Elsevier Ltd. All rights reserved.

1. Introduction

Structural fabrics are used in a wide range of applications, from parachutes to body armor to the protection of structures. Kevlar, which is the most widely used fabric shielding, made its first appearance in bullet-proof vests in the 1970s and is now used extensively. Its high strength-to-weight ratio and flexibility, properties shared by many of the Aramid fabrics, allows its wide use as body armor, such as vests, which can be easily concealed and not encumber or hinder the user. Twaron, Zylon, and a number of other materials have recently been introduced as lighter, but more expensive, alternatives.

In addition to protecting personnel, these fabrics are used in structures and vehicles to stop high-speed projectiles. For the past 15 years, the airline industry has employed ballistic fabrics like Kevlar in the commercial aircraft design. Ever since the crash of flight 232 in 1989 just outside of Sioux City Iowa, aircraft and engine manufacturers have been concerned with rotorburst phenomena. Jet engine manufacturers (such as GE and Rolls Royce) have been using ballistic fabrics to surround the engine turbines in an effort to impede fragments of the rotor that may break off. The Fed-

eral Aviation Administration (FAA) requires each new engine design to pass a rotorburst test before going into service. It should be noted that a single test costs on the order of \$10 million and takes several months to instrument. In addition, the airline manufacturers (Boeing and Airbus) have been using ballistic fabrics in the walls of their commercial aircraft to protect flight critical components in case the engine fails to contain the fragments. Ballistic fabrics such as Kevlar or Zylon are ideal due to their high strength and low weight. The University of California, Berkeley (UCB), has been working with the FAA and the Boeing Company to examine the use of structural fabric as a ballistic shield for commercial aircraft.¹

Since creating and testing an actual aircraft or jet engine is extremely expensive and time consuming, small scale tests and accurate computer models are advantageous to adequately design new aircraft and to validate those designs. In order to accurately capture realistic fabric behavior and failure, discrete models will be employed in this work. Discretely modeling the yarn produces a more realistic model, but is far more computationally expensive. In this work, a multi-scale approach is used where the fabric weave is modeled by a simple network of truss elements. This approach is

* Corresponding author.

E-mail addresses: dpowell1@stanford.edu (D.A. Powell), zohdi@me.berkeley.edu (T.I. Zohdi).

¹ Reports are available through the National Technical Information Service and the FAA [14,21,22,27].

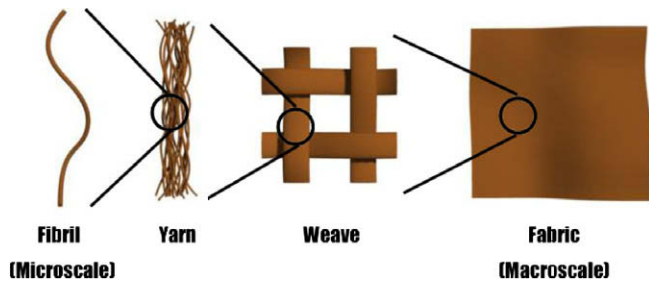


Fig. 1. Multi-scale nature of structural fabric.

able to capture realistic fabric behavior and failure, while significantly reducing the computational cost of the discrete yarn model described above. The number of elements is reduced by a factor of 60 and the number of unknowns by a factor of approximately 210 when compared to a typical yarn-level finite element model (based on mesh shown in Duan et al. [9]). The multi-scale approach relies on purely micro-scale information about the fibrils that make up each yarn.

The goal of this work is to explore the role of boundary attachments during ballistic impact and the effect on the amount of energy absorbed during the impact. Three common attachment methods are explored: (a) fabric pinned near the corners, (b) fabric fixed along two sides and (c) fabric fixed along all four sides. In addition, the role of stochastic-yarn in the model is explored. The weaving process introduces random material variation in every yarn of the fabric sheet. While many models use an average material response, the inclusion of the variation appears to be critical to capturing realistic failure behavior. This work will examine the differences in the predictions of these two approaches.

2. A simple micro-scale fibril/yarn model

In order to accurately capture the behavior of structural fabric without having to resort to phenomenological modeling, a multi-scale approach to fabrics is employed. A sheet of fabric is woven from thousands of yarns, which are themselves comprised of hundreds of micro-scale fibrils (Fig. 1). A macro-scale model for the fabric sheet will be introduced in the following section. This model will be based on the geometry of the fabric sheet and the results of a micro-scale fibril model. This approach allows for a model based entirely on the micro-scale fibril information and thus no macro-scale phenomenological parameters are introduced.

Since the typical quantities of interest involve the global, tensile, force-deflection and, ultimately, fabric rupture, the compressive response is of little interest. For these reasons, we employ a model enforcing a zero stress state for any compressive strains. These types of approaches have been adopted by numerous researchers for the elastostatic analysis of structural fabric; for example Buchholdt et al. [3], Pangiopoulos [17], Bufler and Nguyen-Tuong [4] and Cannarozzi [5,6]. In some cases, such an approach corresponds to so-called relaxed theories of perfectly flexible solids. Pipkin [20] appears to have been the first to have shown that such a model is compatible with the conventional theory of elastic surfaces by considering a minimizing sequence for an associated variational problem, and that such sequences have a structure similar to observed wrinkling in thin elastic sheets. Steigmann and coworkers [1,2,11–13,23] have developed a variety of theoretical results and elastostatic solution techniques based on pseudo-dynamic relaxation methods, such as those found in Papadarakakis [18]. This approach has been applied to the dynamic

analysis of structural fabric and other materials in Zohdi [29], Zohdi and Steigmann [28], and Zohdi and Powell [30].²

3. Fibril description

The micro-scale analysis will begin with a *purely one-dimensional* description of the tensile deformation of the micro-scale fibril. As the fibrils are extremely thin, roughly the width of a human hair, one may assume a uniaxial-stress state of stress. Axial strains for a structural fabric are expected to be in the range of 2–10% prior to rupturing. For example, a Kevlar or Zylon fibril ruptures at approximately a 3% strain [26]. Due to the moderate strains, a simple Kirchhoff–St. Venant material model for the fibrils is reasonable. The stored energy of a single fibril is given by $W = \frac{1}{2}IEE^2$, where IE is Young's modulus, where $E \stackrel{\text{def}}{=} \frac{1}{2}(C - 1)$ is the Green–Lagrange strain, where $C \stackrel{\text{def}}{=} F^T$ is the right Cauchy–Green strain, where $F = \frac{dx}{dX}$ is the deformation gradient, where X are referential coordinates and where x are current coordinates along the axis of the filament. The second Piola–Kirchhoff stress is given by $S = IEE$. During the calculations, it is often more convenient to work with quantities expressed in terms of the stretch ratio, $U = \frac{L}{L_0}$, where L is the deformed length of the fibril, L_0 is its original length and, by virtue of a polar-decomposition, $E = \frac{1}{2}(U^2 - 1)$. For this relaxed one-dimensional model, the Cauchy stress, σ , is related to the second Piola–Kirchhoff stress by $\sigma = \frac{1}{J}F^T S$, where J is the determinant of F and therefore, in one-dimension, $J = F$, thus $\sigma = FS$.

4. Yarn simulation and micro-scale results

The overall response of the yarn is determined by summing the response of each of its individual micro-scale fibrils. For Zylon, a single yarn is made up of 350 individual fibrils. At the micro-scale, unavoidable fibril misalignment occurs due to the weaving process. However, this misalignment is highly advantageous from the standpoint of rupture resistance. In the event that all the fibrils are perfectly aligned, a state that is almost impossible to attain, then one would get instantaneous rupture of the yarn once the critical strain was reached. With misalignment, the axial directions of the fibrils and the yarn are no longer aligned. As such, the rupture of many fibrils will be delayed and the yarn as a whole fails gradually, not suddenly. Another important consequence of the random misalignment of the fibrils is that it is a source of statistical variation for the yarn properties. As the misalignment differs from yarn to yarn, so do the yarn properties. Since each yarn is made up of many fibrils, 350, and not just a few, the differences between yarns tend to be somewhat small. However, as it will soon be shown, the inclusion of these statistical variations, due to the micro-scale fibril misalignment, is critical for accurately capturing the macro-scale behavior.

In order to demonstrate the effects of misalignment, the responses of 100 simulated yarn segments, gripped at the ends, each containing fibrils with different random misalignment, were computed under displacement control. The random orientation of the fibrils was generated with a Matlab random number generator. The distance inclined (with respect to the longitudinal axis of the yarn), d_j , was randomly chosen using a Gaussian distribution with a standard deviation of half the width of the yarn. According to the manufacturer (of Zylon), each fibril has a Young's modulus of $IE_f = 180$ GPa, the stretch at failure is $U_{crit} = 1.03$, and there are 350 fibrils in a single yarn.³ The misalignment was generated by

² Although we do not discuss continuum models here, they have also received attention in the last few years for modeling structural fabric. We refer reader to Tabiei and Jiang [24], Lim et al. [15,16], Cheeseman and Bogetti [7], Phoenix and Porwal [19], Shockey et al. [22], Tan et al. [25], Duan et al. [8–10], among others.

³ We used data specific to Zylon, which was provided by the FAA for research purposes.

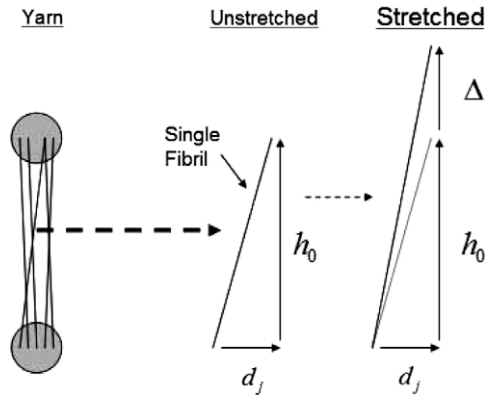


Fig. 2. Stretching of a single fibril.

randomly orienting (leaning) the fibrils according to the measured thickness of Zylon yarn which are relatively flat. The amount of inclination and initial fibril length were determined by placing the fibrils within a hypothetical (tubular) yarn domain with an elliptical cross-sectional area. The cross-sectional area had a minor radius of $r = 0.000185$ m and aspect ratio of 4:1, leading to a major radius of $r = 4 \times 0.185$ mm. The separation distance of the two yarn end-points was $h_0 = 0.725$ mm (Fig. 2).

In Fig. 3 one can see the response of 100 simulated yarn with random misalignment of the fibrils and one yarn with no misalignment (i.e. all fibrils perfectly aligned). It is clear that without misalignment the yarn would be stiffer as the yarn's elastic modulus with misalignment is less than the modulus of a fibril. However, without misalignment, rupture would be sudden, as all fibrils would rupture at the same strain. Despite the higher (peak) stress at failure, there is a larger area under the curve for the yarn with misalignment. This means that the yarn with misaligned fibrils absorbs a greater amount of energy prior to total failure than a yarn with perfectly aligned fibrils. Again, it is clear that including the micro-scale fibril misalignment is essential to accurately modeling the macro-scale fabric sheet. The material has a more gradual, realistic rupture behavior, which is a natural outcome of the multi-scale model. Furthermore, this misaligned response is in excellent agreement with the experimental results furnished by the Boeing Company [27], which are shown in Fig. 3. The resulting stiffness, failure stress, and general failure behavior are all in good agreement with Boeing's tests on actual Zylon yarn segments.

The response of a yarn can be stated explicitly. For an individual j th fibril, the stretch is equal to $U_j = \frac{L_j}{L_{j0}}$, where L_j is the deformed length of the fibril and L_{j0} is its original length. The axial stretch can be rewritten as

$$U_j = \frac{L_j}{L_{j0}} = \frac{\sqrt{(h_0 + \Delta)^2 + d_j^2}}{\sqrt{h_0^2 + d_j^2}} \quad (1)$$

where h_0 is the initial length of the yarn, nominal distance between suture points, d_j is the length of misalignment for the j th fibril, and Δ is the displacement of the yarn's end points. For the l th yarn, containing N_l fibrils, the effective axial second Piola–Kirchhoff response (per yarn) can be written in terms of the fibril deformation and its material properties

$$S_l = IE_l^* \frac{1}{2} \left(\frac{(h_0 + \Delta)^2}{h_0^2} - 1 \right) = \frac{1}{N_l} \sum_{j=1}^{N_l} IE_f \frac{1}{2} \left(\frac{(h_0 + \Delta)^2 + d_j^2}{h_0^2 + d_j^2} - 1 \right) \frac{h_0}{\sqrt{h_0^2 + d_j^2}} \xi_j \quad (2)$$

where IE_f is the Young's modulus of a fibril, where IE_l^* is the effective Young's modulus of the yarn, where (I) $d_j = d_0 \lambda_j$, where λ_j is a random number such that $0 \leq \lambda_j \leq 1$, and where d_0 is the maximum horizontal inclination possible for a fibril (Fig. 2), (II) $\xi_j = 1$ if $U_j < U_{crit}$ and (III) $\xi_j = 0$ if $U_j \geq U_{crit}$ and where U_{crit} is a critical uniaxial stretch. This leads to

$$IE_l^* = \frac{IE_f h_0^3}{N_l} \sum_{j=1}^{N_l} \frac{1}{(h_0^2 + d_j^2)^{3/2}} \xi_j \quad (3)$$

For a more detailed discussion of this model, see Zohdi and Powell [30].

5. Macro-scale fabric sheet model

For the coarse weave of many structural fabrics, treating the sheet as a continuum is not a useful model. In this case, the diameter of the projectile is less than 20 yarns across. Thus, the choice was made to model the yarn discretely as continuous truss elements connecting a network of lumped masses (Fig. 4). The macro-scale model begins with an initially undeformed two-dimensional network of yarn made up of micro-scale fibrils. The yarn are pinned together at nodes. In reality the yarn are tightly woven, not pinned. The nodes are placed at every criss-cross contact junction between the warp and the fill of the weave.

The macro-scale model is relatively straightforward to implement. The truss network can be solved directly or as part of a finite element model. Either an implicit or explicit method for solving the nonlinear ODEs would be acceptable. The results presented in this work make use of the trapezoidal rule (an implicit method). The nonlinear equations were solved using a simple fixed-point iteration. The advantage of the specific type fixed-point iteration employed is that no matrix equation needs to be solved; the system of equations can instead be solved rapidly in (node by node) vector form. For additional details on this implementation see Zohdi and Powell [30].

6. Yarn–fibril homogenization

While the micro-scale simulation can compute the yarn response very quickly, it calculates the responses one at a time; calculating the full response of a single yarn before moving on to the next yarn, and so forth. Calculating the response of many yarn simultaneously can be extremely memory intensive. For a single yarn, the inclination of each fibril must be stored as well as a flag denoting whether or not a given fibril has failed. As a single yarn has 350 individual fibrils, storing the inclination information of each fibril means storing 350 pairs of information. In a 10 by 10 in. sheet, such as the ones used for testing at UCB, there are approximately 244,300 yarn. Computing the micro-scale simulation during the macro-scale calculation requires storing 171,010,000 constants.

A significant reduction in the computational effort can be achieved by first precomputing the mean, maximum and minimum for a population of yarn over the entire possible deformation range, and then reconstructing a constitutive response “on the fly” (during the computations) for each yarn. This can be done either by accessing an embedded precomputed stretch–response “database” or creating a constitutive law based on the data with parameters from a least squares calculation. In order to speed up the computations, the latter was chosen. This allows the algorithm to store only two constants (Young's modulus and damage rate parameter) and one history variable (total damage) per yarn. This significantly reduces the storage space and computational effort required to run the macro-scale simulation. Furthermore, the macro-scale

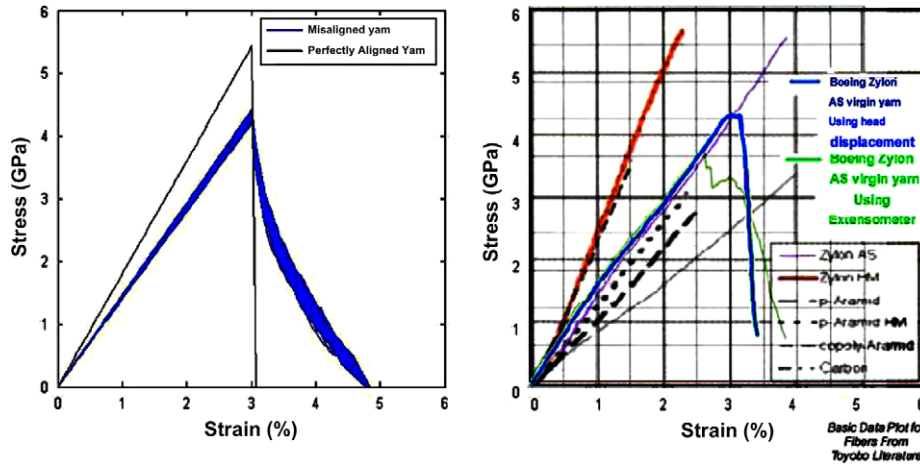


Fig. 3. (Left) Simulated response of 100 yarn based on randomly oriented micro-scale fibrils and one yarn with perfectly aligned fibrils. (Right) The blue line is the stress-strain response for a Zylon yarn as measured by the Boeing Corporation [27]. (For interpretation of the references to color in this figure legend, the reader is referred to the web version of this article.)

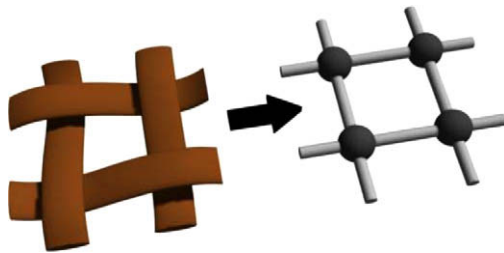


Fig. 4. Truss network with lumped mass nodes representing the yarn of the macro-scale fabric sheet.

simulation only affects the micro-scale simulation by providing it with the current (yarn) stretch. There are no complicated changes to a single yarn's geometry that need to be included. Thus, there would be no benefit to the method by simulating the micro-scale at each time step to offset the additional memory and computational time requirements.

To model the yarn response, a simple Kirchhoff–St. Venant material model, $S = IEE$, was used where the weakening of the material was introduced through IE . Thus, $IE(U, t) = \alpha(U, t)IE_0$. IE_0 is the undamaged Young's modulus and is a constant assigned to each yarn. Due to fibril misalignment, this value is statistically determined for a specific yarn and will vary over the fabric. $\alpha(U, t)$ is the measure of the damage in the yarn (due to ruptured fibrils) and causes a weakening (reduction) in IE as more and more of the fibrils fail. IE_0 is found by first taking the mean value of IE from the earlier micro-scale computation and then perturbing it by some amount. This perturbation produces a different value of IE_0 for every yarn. Multiple runs of the micro-scale simulation produce the Gaussian distribution shown in Fig. 5. Accordingly, IE_0 will differ for every yarn with no preference to the yarn's location or to the values possessed by the yarn's neighbors.

The variable α is the damage in each yarn. As fibrils rupture, α goes from unity, corresponding to an undamaged yarn, to zero, a yarn that has failed completely. α is obviously a function of the strain, but it is also a function of history of the yarn. After a yarn has been damaged, reducing the strain will not reattach snapped fibrils. Thus

$$\alpha(U, t) = \min(\hat{\alpha}(U), \alpha(U, t - \Delta t)) \tag{4}$$

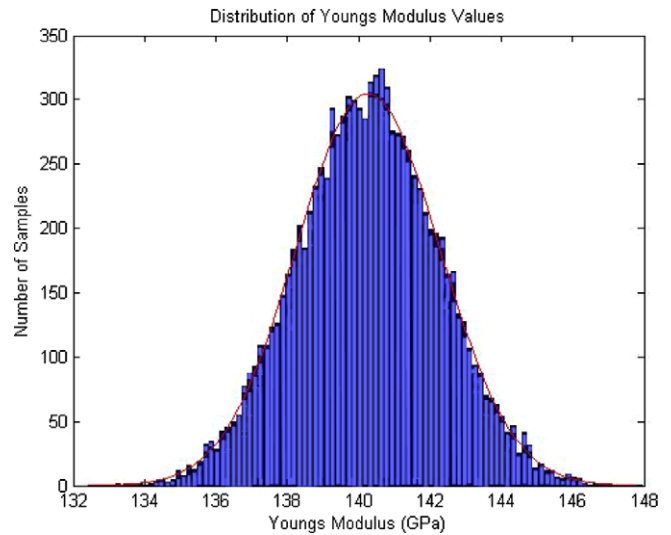


Fig. 5. Distribution of Young's modulus based on 10,000 runs of the micro-scale simulation.

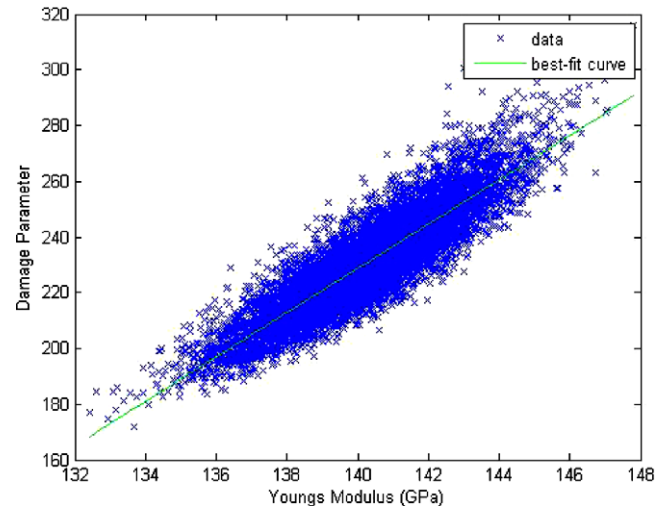


Fig. 6. Distribution of the damage parameter, λ , as a function of Young's modulus values based on 10,000 runs of the micro-scale simulation.

Here $\alpha(U, t - \Delta t)$ is the damage in the yarn at the previous moment in time. The damage evolution behavior is similar to exponential decay, so the following equation was used for $\hat{\alpha}$:

$$\hat{\alpha}(U) = A(\exp^{-\lambda(U-U_{crit})} - B) \quad (5)$$

where the values of A , B , and λ were determined by fitting the curve to the data and using a least squares best fit. Fig. 6 shows the distribution of λ values versus the Young's modulus of the yarn. There is clearly a correlation between the stiffness of the yarn and the rate at which the damage grows. When assigning λ values in the simulation, a Gaussian distribution was used where the mean value was assumed linearly dependent on the Young's modulus (based on Fig. 6).

7. Contact

Consistent with the cited experimental data, the problem of interest is the resistance to puncture of initially planar sheets of fabric by a projectile. In order to simplify the problem somewhat, it is assumed that the penetrator is rigid. The fabric deformations are finite and involve a certain amount of randomness due to material variation, therefore all nodes can potentially come into contact with the projectile during the course of the simulation. The search to determine if a node is in contact with the projectile depends on the shape of the projectile.⁴ If the projectile is a more complicated shape, such as a cylinder with a flat or hemispherical end, then the determination of contact requires several more steps. The fabric's nodes must be checked against penetration of the specific surface of the projectile.

Contact is enforced using a Lagrange multiplier method. The interaction between the projectile and fabric is assumed to be frictionless. As a result, the contact force will be normal to the surface of the projectile. The magnitude of the contact force can then be determined by considering it to be the value necessary to prohibit interpenetration of the projectile by the nodes. The resulting non-linear equations can be solved using a simple fixed-point iteration.

8. Projectile motion

As the positions of the nodes are changed to enforce contact, the force required to cause this change is calculated. An equal and opposite force must also be applied to the projectile. The projectile is a three-dimensional body, so torques caused by the fabric–projectile interaction must also be taken into account. The interaction force due to the i th node, f_{pi} , is applied at r_i , the contact point on the projectile's surface. The moment about the center of the projectile due to this force is $M_{pi} = r_i \times f_i$. As the projectile is very stiff compared to the fabric, it is treated as a rigid body, and thus it is assumed not to deform, but only to undergo rigid-body translation and rotation. For the motion of the projectile's center of mass, the net force on the projectile is given by

$$m_p \ddot{u}_p = \sum f_{pi} \quad (6)$$

where m_p is the mass of the projectile, u_p is the position of the projectile, and f_{pi} is the force from the i th node on the projectile. For the orientation of the projectile, the sum of the moments equals the change in angular momentum.

$$\frac{d}{dt}(I_p \cdot \omega_p) = \sum M_{pi} \quad (7)$$

where I_p is the projectile's moment of inertia, ω_p is the angular velocity of the projectile, and M_{pi} is the applied torque or moment

due to the i th node's interaction with the projectile. Both the projectile's angular velocity and moment of inertia change during the motion. Therefore, Eq. (7) can be rewritten as

$$\dot{I}_p \cdot \omega_p + I_p \cdot \dot{\omega}_p = \sum M_{pi} \quad (8)$$

However recalculating the moment of inertia at each time step is inconvenient. Therefore, the moment of inertia and the projectile's angular momentum can be described in terms of a basis that is fixed to the projectile (Fig. 7), leading to

$$\begin{aligned} I_p \cdot \omega_p &= I_{p1} \omega_{p1} e_1 + I_{p2} \omega_{p2} e_2 + I_{p3} \omega_{p3} e_3 \\ &= I'_{p1} \omega'_{p1} a_1 + I'_{p2} \omega'_{p2} a_2 + I'_{p3} \omega'_{p3} a_3 = I'_p \cdot \omega'_p \end{aligned} \quad (9)$$

Here e_j is the basis fixed to the observer's reference frame, a_j is the basis fixed to the projectile's reference frame, and \cdot denotes a quantity defined on the a_j basis (Fig. 8). The I'_{pi} 's are constant throughout the motion, but each a_j will change. Since a_j are attached to the body, $\dot{a}_j = \omega'_p \times a_j$. Thus, Eq. (7) can be rewritten as

$$\frac{d}{dt}(I'_p \cdot \omega'_p)_{rot} + \omega'_p \times I'_p \cdot \omega'_p = \sum M_{pi} \quad (10)$$

Here $\frac{d}{dt}(\cdot)_{rot}$ is the time derivative in the rotating reference frame. Alternatively, Eq. (10) can be written in component form as

$$I'_{p1} \dot{\omega}'_{p1} + (I'_{p3} - I'_{p2}) \omega'_{p2} \omega'_{p3} = \sum M'_{pi1} \quad (11)$$

$$I'_{p2} \dot{\omega}'_{p2} + (I'_{p1} - I'_{p3}) \omega'_{p3} \omega'_{p1} = \sum M'_{pi2} \quad (12)$$

$$I'_{p3} \dot{\omega}'_{p3} + (I'_{p2} - I'_{p1}) \omega'_{p1} \omega'_{p2} = \sum M'_{pi3} \quad (13)$$

Both approaches for determining the projectile's orientation, 7 and 10, are acceptable. From a coding standpoint, 10 was deemed the simpler option. It should be noted, that for a spherical projectile the interaction forces between the projectile and the fabric, which are always normal to the projectile's surface, will produce zero torque. Thus only the translation of the projectile needs to be determined. If friction between the projectile and the fabric was included, then this would no longer be true.

To solve the resulting equations, we can rewrite 11 as

$$\dot{\omega}_{p1} = \frac{1}{I_{p1}} \left(\sum M_{pi1} - (I_{p3} - I_{p2}) \omega_{p2} \omega_{p3} \right) \quad (14)$$

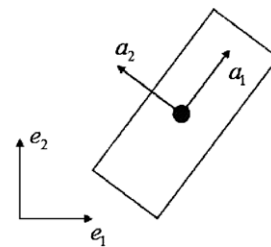


Fig. 7. Reference basis, e_i , and basis, a_i , fixed to projectile.

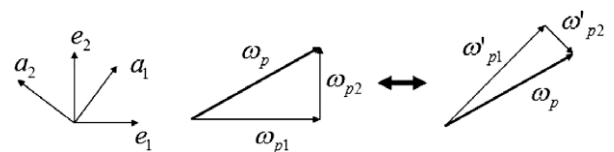


Fig. 8. Angular velocity vector resolved on both coordinate systems.

⁴ For example, for a sphere, the search is simple. The distance from a node to the center of the projectile must be greater than or equal to the radius, R , of the projectile.

For simplicity, the primes have been dropped. This is a first order ordinary differential equation. As with the equations for the motion of the nodes, this equation can be solved using the theta rule

$$\begin{aligned} \omega_{p1}(t + \Delta t) = & \omega_{p1}(t) + \frac{\Delta t}{I_{p1}} \left(\theta \sum M_{pi1}(t + \Delta t) + (1 - \theta) \sum M_{pi1}(t) \right) \\ & - \frac{\Delta t}{I_{p1}} (I_{p3} - I_{p2}) (\theta \omega_{p2}(t + \Delta t) \omega_{p3}(t + \Delta t) \\ & + (1 - \theta) \omega_{p2}(t) \omega_{p3}(t)) \end{aligned} \quad (15)$$

Eq. (15) is a nonlinear equation so it will be solved using fixed-point iteration

$$\begin{aligned} \omega_{p1}^K(t + \Delta t) = & \omega_{p1}(t) + \frac{\Delta t}{I_{p1}} \left(\theta \sum M_{pi1}^{K-1}(t + \Delta t) + (1 - \theta) \sum M_{pi1}(t) \right) \\ & - \frac{\Delta t}{I_{p1}} (I_{p3} - I_{p2}) \left(\theta \omega_{p2}^{K-1}(t + \Delta t) \omega_{p3}^{K-1}(t + \Delta t) \right. \\ & \left. + (1 - \theta) \omega_{p2}(t) \omega_{p3}(t) \right) \end{aligned} \quad (16)$$

where K is an iteration counter. The same approach is taken when developing the equations for ω_{p2} and ω_{p3} .

9. Results and discussion

In order to evaluate the performance of the numerical model, simulations were run matching the setup and initial conditions to those of the experimental tests run at UCB. The simulation modeled a 50 caliber (0.0127 m or 0.5 in. diameter) cylindrical projectile with a mass of 0.037 kg and a length of 0.0381 m (1.5 in.) impacting the fabric sheet. An initially planar, square, fabric target with dimensions 0.254 by 0.254 m (10 by 10 in.) was chosen. The spacing of truss elements was set to match the yarn spacing (1378 yarn per meter or 35 yarn per inch). Consequently 350×350 lumped mass nodes and $3 \times 350 \times 350 = 367,500$ degrees of freedom or unknowns were needed for the computations. The diameter for each of the fibrils that make up the yarn is estimated to be 0.02 mm. The cross-sectional area for the yarn was determined by summing the areas of all of the fibrils making up that yarn, thus each yarn would have a cross-sectional area of $1.075 \times 10^{-7} \text{ m}^2$. The mass of the entire 10 in.² fabric sheet was measured to be 7.99 g. Based on this information, the mass of a single node was determined to be $6.52 \times 10^{-8} \text{ kg}$.

Guided by the micro-scale simulation, the overall mean stiffness of the yarn was determined to be $IE_{mean}^* = 140.21 \text{ GPa}$ with a standard deviation of 2.04 GPa. As discussed earlier, the mean value of the damage parameter λ for a given yarn is linearly dependent on the value of that yarn's Young's modulus. Using a least squares approach, the dependence was determined to be

$$\lambda_{mean} = (7.91(1/\text{GPa})) * IE_i - 878.46 \quad (17)$$

where λ_{mean} is unitless and IE_i is measured in GPa. The standard deviation for λ was determined to be 8.35.

Simulations were run on a standard Dell workstation with a research code written in Fortran 90. The total simulation time was on the order of 10 min.

10. Comparison of numerical and experimental results

A number of different boundary conditions were examined in the experimental tests performed at UCB. One common set of boundary conditions involved clamping the fabric along two opposing sides. To recreate this boundary condition in the simulation, all nodes along the corresponding boundaries are held fixed ($u_i(t) = u_i(0)$). Of course this differs slightly from the experiments in that absolutely no motion of the boundary nodes is permitted. In

the experiments, there would be some sliding at the boundaries. However, this sliding is assumed to be small enough to ignore.

Fig. 9 shows a series of four images taken from the high-speed video of the experiment. The video is shot in profile and shows the fabric mount in all four images. The projectile can be seen entering from the right and moving towards the left. During the test the fabric deforms slightly and then fails at the center, the point of impact. The image is zoomed in towards the point of impact and the fabric sheet extends far beyond what is shown.

Fig. 10 shows a series of four images taken from the numerical simulation of the fabric sheet. The predicted deformation and failure region agree with the experimental results.

A second common set of boundary conditions involved pinning the fabric at each of its corners. In this case, a small hole was cut at each of the corners, 1 in. from the sides. A bolt was slipped through the hole and the fabric was held in place by a 1.5 in. diameter washer, fixing it to the mount. To recreate this boundary condition in the simulation, all nodes within the area of the washer were held fixed. Fig. 11 shows a series of four images taken from the high-speed video of the experiment. As before, the video is shot in profile and shows the fabric mount in all four images. The projectile can be seen entering from the right and moving towards the left. Unlike the previous image series, with these boundary conditions the fabric deforms significantly. Failure occurs at the boundaries, occurring first at the upper two corners followed by the lower two.

Once again, a numerical simulation was run with initial conditions set to match the experiment. Fig. 12 shows a series of four images taken from the numerical simulation. Unlike the previous simulation, the deformation is much larger and failure occurs at the boundaries. And, as in the experiment, failure does not occur at all boundaries simultaneously.

In both of these cases, the simulation and the experiment agree qualitatively very well. The correct deformation in the sheet is predicted by the model as well as the location and the behavior of the failure mechanism for the sheet. It is important to note that no parameters have been changed to cause the simulation and the experiment to agree. All parameters are determined by the geometry of the fabric and the results of the micro-scale simulation. The only changes made to the simulation were to adjust the boundary

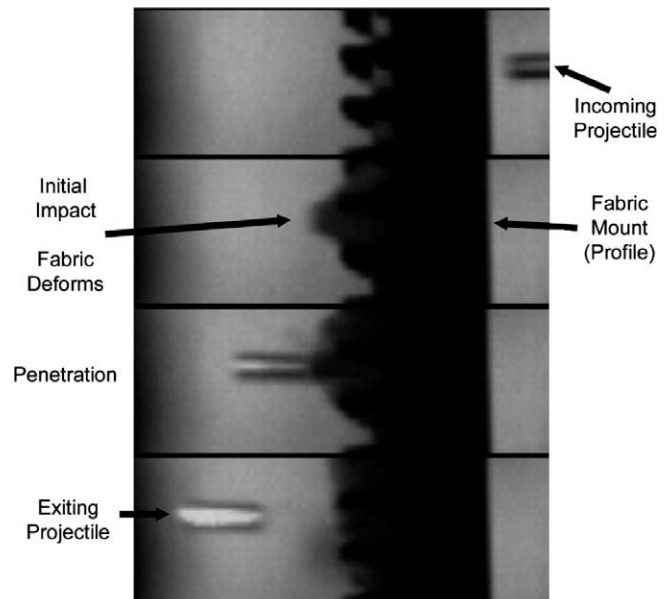


Fig. 9. Series of images from high-speed video of experimental test. Fabric clamped on two sides.

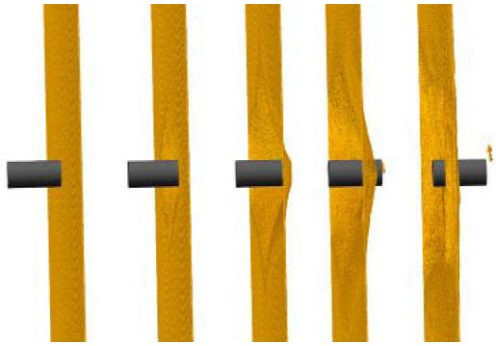


Fig. 10. Series of images from numerical simulation of fabric clamped on two sides.

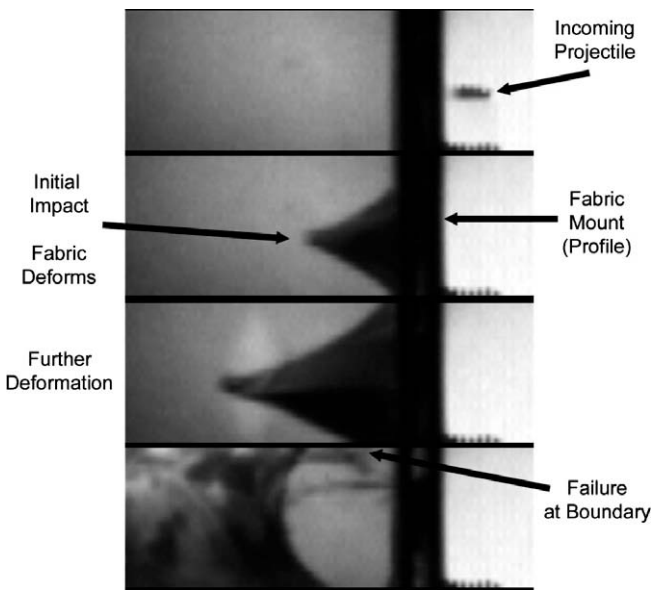


Fig. 11. Series of images from high-speed video of experimental test. Fabric pinned at the corners.

conditions. Despite the good qualitative agreement, a quantitative comparison is still desirable. In the experiments, the initial and residual velocities of the projectiles were measured. The initial velocity was determined as the projectile passed through a series of laser gates. Due to the erratic path of the projectile after the impact, the high-speed video was used to calculate the residual velocity of the projectile. Fig. 13 shows the residual velocity of the projectile versus the initial velocity. Both the data collected from the experiment and data collected from the simulation are shown. The simulation and the experiment are in good agreement, espe-

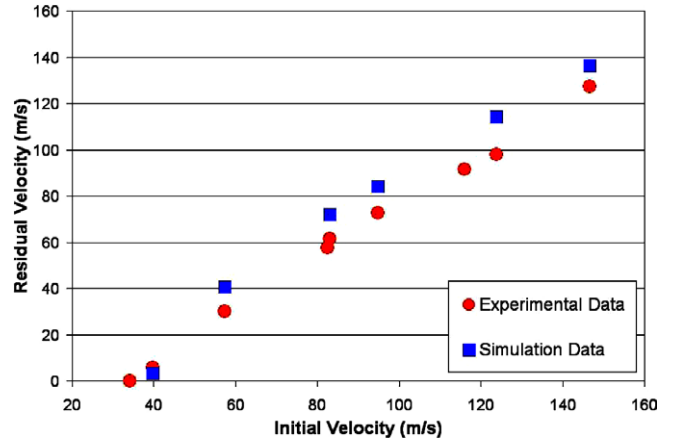


Fig. 13. Comparison of experimental and numerical test results, projectile's residual velocity as a function of initial velocity shown.

cially at the lower range where the residual velocity approaches zero. At higher velocities, the simulation slightly over-predicted the residual velocity of the projectile. Friction most likely accounts for the additional energy loss seen in the experimental results. Work is currently being done to include friction in this model.

11. Effect of boundary conditions on energy absorption

With confidence in the numerical simulation, the role of boundary conditions can now be examined. Three different boundary conditions are of interest: fabric pinned at the corners, fabric clamped along two sides, fabric clamped along four sides. The first two of these boundary conditions were described above. The third, fabric clamped along all four sides, is merely an extension of the two sides boundary condition. For ballistic shielding, the primary role of these fabrics is to strip energy away from the projectile. Consequently, the amount of energy absorbed as a function of the initial energy is of primary interest. The question we are trying to answer is which type of boundary attachment results in the greatest amount of energy absorption and why.

The following series of results were created using a simulation as described above with a few minor changes. The shape of the projectile was changed to a sphere with a 0.0127 m or 0.5 in. diameter and a mass of 8.4 g. These values are used to match another projectile used in the testing at UCB. The spherical projectile was chosen so as to reduce any variation in the results due to tumbling. All of the energy of the projectile is in translational kinetic energy; none in rotational kinetic energy. The other change was to reduce the size of the simulated sheet to 0.0762 m (3 by 3 in.). In addition to reducing the time needed for each simulation, the decrease in the size of the sheet should amplify the role of boundary conditions during the impact.



Fig. 12. Series of images from numerical simulation of fabric pinned at the corners.

When interpreting the results, it is important to keep in mind that variation at the micro-scale, fibril misalignment, is included in the macro-scale simulation producing a stochastic-yarn model. In effect, every time the simulation is run a different random fabric sheet is generated. As a consequence, the results of a single simulation do not provide the average response. The simulation must be repeated using the same initial conditions. Of primary interest is the amount of energy the fabric sheet strips off of the projectile during impact. Fig. 14 shows the average energy absorbed by a single sheet of fabric as a function of the projectile's initial energy. All three sets of boundary conditions are shown in the figure. At the lower end of the range, where the majority of the energy is absorbed, all three boundary conditions are relatively close. At the higher end of the range, the fabric pinned at the corners begins to absorb a significantly larger amount of energy. This will be explored in more depth shortly. From this plot, it can be clearly seen that the fabric fixed along two sides absorbs the least amount of energy while fabric pinned at the corners absorbs the most.

Figs. 15–17 show a more detailed look at the energy in the system during impact for the fabric fixed along four corners, two sides, and four sides, respectively. In each plot the total amount of kinetic energy lost by the projectile is shown versus time as well as the kinetic energy and strain energy in the fabric sheet. The fabric fixed along all four sides is allowed the least amount of free movement

and thus the majority of energy absorbed goes into deforming the fabric or the strain energy of the fabric sheet. The fabric fixed along two sides is allowed more movement and thus more energy is transferred from the projectile into kinetic energy in the fabric. However, as two sides of the sheet are no longer constrained, the amount of strain energy absorbed by the fabric sheet is reduced. For the fabric sheet fixed at the corners, the greatest amount of deformation is seen in the experimental and numerical results. As expected, the amount of energy lost to the kinetic energy of the fabric is significantly higher, almost by a factor of three, than the other two cases. Meanwhile, the strain energy remains consistent with the values seen in the other simulations.

12. Role of material variation

It has been stated that this approach, because of the inclusion of material variation, requires multiple runs for each set of initial conditions in order to produce the average response of the fabric sheet. Since the inclusion of this variation requires additional work in order to produce results, one could question if it is necessary. In order

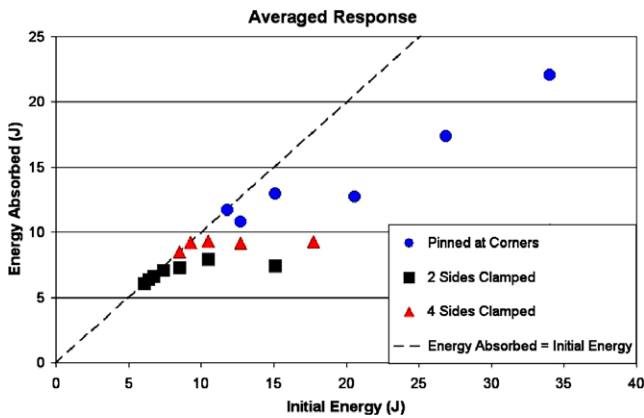


Fig. 14. Average energy absorbed by fabric sheet for each of the three boundary conditions.

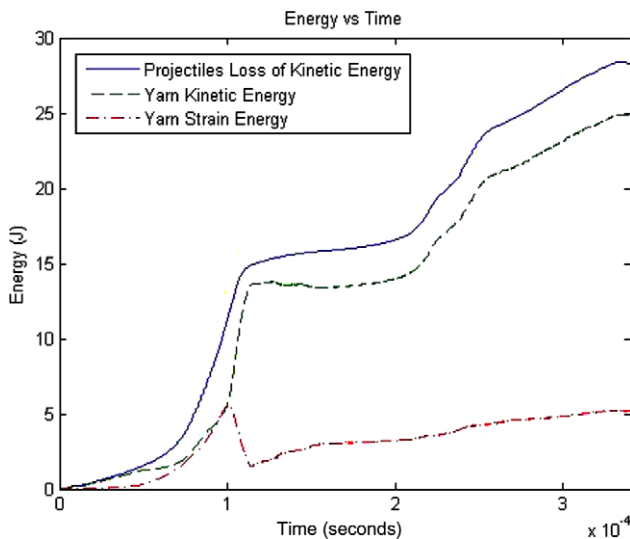


Fig. 15. Energy in the system during impact of fabric pinned at the corners.

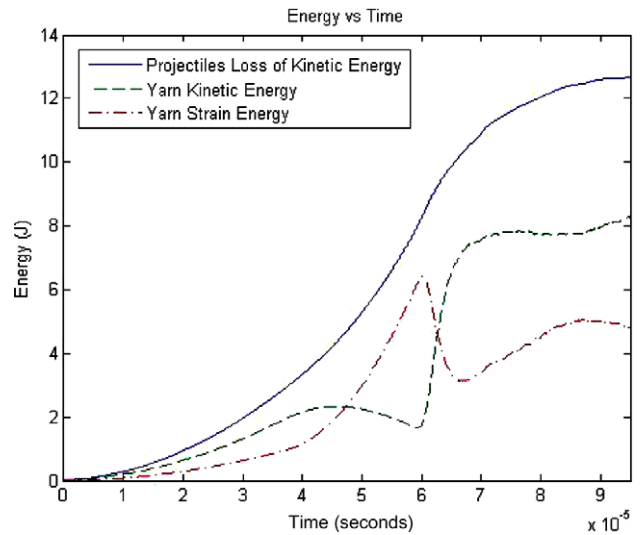


Fig. 16. Energy in the system during impact of fabric clamped on two sides.

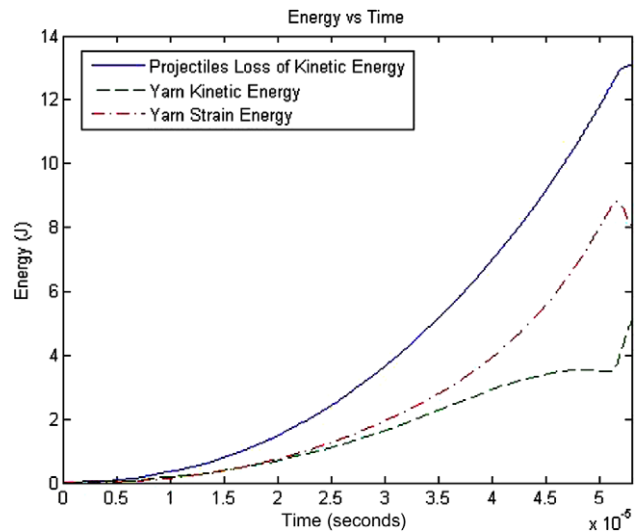


Fig. 17. Energy in the system during impact of fabric clamped on four sides.

to answer this, we must explore the affect of including stochastic-yarn in the model or artificially imposed uniform-yarn in the model on the numerical results. Most numerical models of ballistic fabric use an average material response for all of the yarn. This uniform-yarn model has a number of geometric symmetries that can be exploited to reduce the size of the problem and speed up simulation time. This model presented here is easily adapted to create a uniform-yarn sheet of fabric by setting the Young's modulus in every yarn to the mean value of 140.21 GPa and the damage parameter to a corresponding mean value of 230.6. Planes of symmetry can also be introduced to reduce the number of unknowns and reduce the computation time. These series of simulations were then repeated for each of the boundary conditions.

Fig. 18 shows the response of the uniform-yarn fabric sheet side by side with the averaged response of the stochastic-yarn sheet for the fabric pinned at the corners. While the two data sets are similar at the higher end of the range, there is significant divergence near the ballistic limit. The uniform-yarn model over-predicts the amount of energy absorbed by a factor of 2. One of the main causes for this discrepancy may be the modes of failure allowed by each model. In the stochastic-yarn model, impacts with lower initial energy cause only one or two of the boundary attachments to fail. The projectile then pushes the fabric sheet out of the way without causing the remaining boundary attachments to fail. With this type of failure, the sheet absorbs less energy in the form of strain energy or work done by the yarn. When failure occurs in the uniform-yarn sheet, on the other hand, all four boundary attachments will always fail regardless of the initial energy of the projectile. The energy absorbed in the form of strain energy can be as much as 2–4 times as large in the uniform-yarn sheet as in the stochastic-yarn sheet. At higher initial energies, all four boundary attachments typically fail in the stochastic-yarn model. In this range, the two models are in much greater agreement.

Figs. 19 and 20 show the response of the uniform-yarn fabric sheet side by side with the averaged response of the stochastic-yarn sheet for the fabric clamped on two and four sides, respectively. In both cases the uniform-yarn model slightly over-predicts the energy absorbed by the fabric sheet. Unlike the previous boundary condition, the failure in the sheet occurs in the center and does not change significantly over the range of initial energies. Still, there are differences in the failure pattern of the two models. In the uniform-yarn model, all yarn are identical, so failure occurs in yarn at either two or four points along the primary directions depending on the planes of symmetry. In the stochastic-yarn model, failure initiates at weak points in the fabric near the contact re-

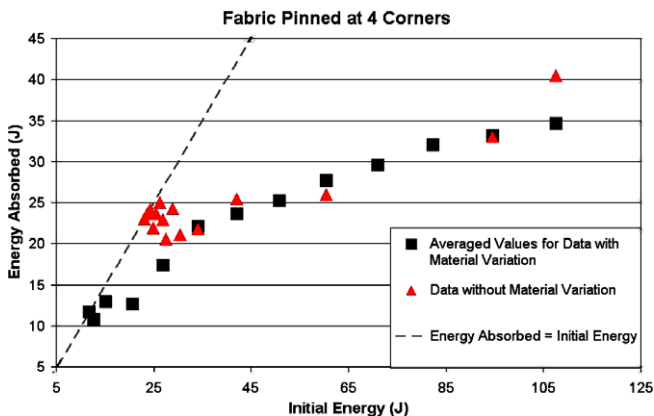


Fig. 18. Energy absorbed by the fabric sheet pinned at the four corners. Average response of the stochastic-yarn sheet and the response of the uniform-yarn sheet are shown.

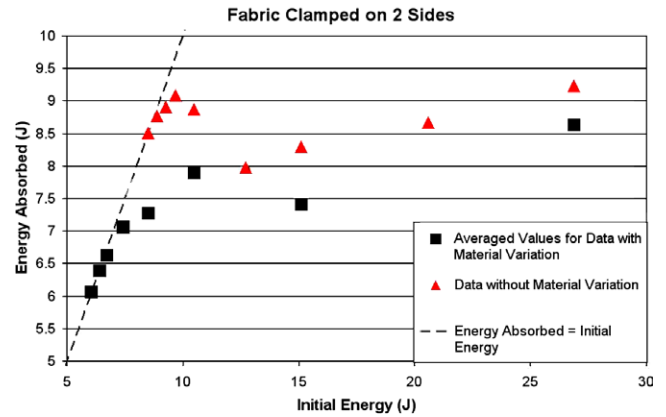


Fig. 19. Energy absorbed by the fabric sheet clamped along two sides. Average response of the stochastic-yarn sheet and the response of the uniform-yarn sheet are shown.

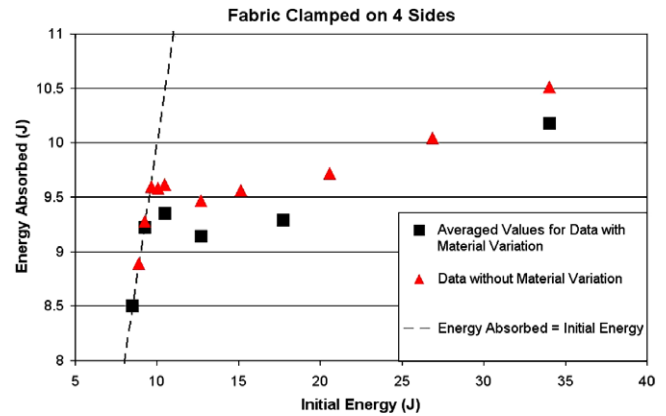


Fig. 20. Energy absorbed by the fabric sheet clamped along four sides. Average response of the stochastic-yarn sheet and the response of the uniform-yarn sheet are shown.

gion. Consequently, slightly less energy is absorbed in the stochastic-yarn sheet, as seen in both plots.

13. Conclusion

The model presented in this work takes a multi-scale approach to modeling structural fabric based on a network of yarn with stochastic properties determined by smaller-scale fibrils, which are randomly misaligned. By using purely micro-scale information to build the model (simply measuring the properties of an individual, smallest-scale fibril), all necessary material parameters are easily verifiable and no phenomenological parameters are required. It is important to emphasize that the properties of a fibril are easily ascertained from a simple tension test. The use of simple truss elements to represent the yarn created a model that naturally captures the fabric behavior needed in ballistic regimes. Additionally, as individual yarns are allowed to break in the model, more realistic failure behavior is achieved. The response of the overall fabric model and ballistic experiments are in excellent agreement. The model indicates that fabric which is attached by being pinned at the corners generally absorbs more energy, relative to fabric clamped along the sides. The basis for this result is discussed at length. The effects of stochasticity on the overall response were investigated. Furthermore, it is observed that a uniform-yarn model, one which ignores the stochastic nature of the yarn, over-estimates the amount of energy absorbed.

Material variation in the yarn caused by the micro-scale misalignment of the fibrils is critical to accurately capturing the fabric behavior. By artificially imposing uniformity of the yarn on the fabric sheet, failure modes seen in experiment tests cannot be reproduced by the model. The inclusion of stochastic-yarn in the macro-scale model is important, and is a key feature that allows the numerical results to closely match the experimental results over the range of boundary conditions examined. In addition, the uniform-yarn model consistently over-predicts the amount of energy absorbed during impact. This is especially hazardous in the case of ballistic shielding where accurate measurements of energy absorbed are critical to designing safe shielding.

Of the three major boundary conditions examined, the fabric pinned at the corners absorbed the greatest amount of energy. The majority of the energy lost by the projectile was transferred into the kinetic energy of the fabric. In large part, this was due to the large deformation allowed by this specific boundary attachment. This may be suitable in some applications such as ballistic shielding for some vehicles and structures, but not suitable as shielding for personnel or other vehicles where space is limited. The fabric clamped along the sides absorbed less energy, but also had significantly smaller deformation. The majority of the energy lost by the projectile was transferred into the strain energy of the fabric.

For the comparison between the uniform-yarn and stochastic-yarn models, the fabric pinned at the corners had the largest discrepancy in the results. Near the ballistic limit, the stochastic-yarn model would fail at only some of the boundary attachments, as supported by the experimental results. The uniform-yarn model, due to the imposed symmetry, always had failure at all four boundary attachments. The fabric sheets clamped along the side always failed at the center, a type of failure that could be reproduced in the uniform-yarn model. While the failure in the stochastic-yarn sheet would initiate at slightly different locations and produce different hole patterns, the damage seen in the sheet was of a more symmetric nature than the damage in the sheets pinned at the corners. As a result, the uniform-yarn and stochastic-yarn model differed by a significantly smaller margin for the clamped sides boundary conditions. Still, due to subtle differences in the fabric sheet, the uniform-yarn model continued to over-predict the amount of energy absorbed during impact. In all cases, the model including material variation at the macro-scale is a more reliable modeling approach.

Acknowledgements

This work was funded in part by the Federal Aviation Administration through the Aircraft Catastrophic Failure Prevention Program (cooperative agreement 01-C-AW-UCB and FAA Grant 2007-G-005), the Army Research Laboratory through the Army High Performance Computing Research Center (cooperative agreement W911NF-07-2-0027) and the Powley foundation.

References

- [1] Atai AA, Steigmann DJ. On the nonlinear mechanics of discrete networks. *Arch Appl Mech* 1997;67:303–19.
- [2] Atai AA, Steigmann DJ. Coupled deformations of elastic curves & surfaces. *Int J Solids Struct* 1998;35(16):1915–52.
- [3] Buchholdt HA, Davies M, Hussey MJL. The analysis of cable nets. *J Inst Math Appl* 1968;4:339–58.
- [4] Bufler H, Nguyen-Tuong B. On the work theorems in nonlinear network theory. *Ing Arch* 1980;49:275–86.
- [5] Cannarozzi M. Stationary & extremum variational formulations for the elastostatics of cable networks. *Meccanica* 1985;20:136–43.
- [6] Cannarozzi M. A minimum principle for tractions in the elastostatics of cable networks. *Int J Solids Struct* 1987;23:551.
- [7] Cheeseman BA, Bogetti TA. Ballistic impact into fabric and compliant composite laminates. *Compos Struct* 2003;61:161–73.
- [8] Duan Y, Keefe M, Bogetti TA, Cheeseman BA. Modeling the role of friction during ballistic impact of a high-strength plain-weave fabric. *Compos Struct* 2005;68:331–7.
- [9] Duan Y, Keefe M, Bogetti TA, Cheeseman BA. Modeling friction effects on the ballistic impact behavior of a single-ply high strength fabric. *Int J Impact Eng* 2005;31:996–1012.
- [10] Duan Y, Keefe M, Bogetti TA, Powers B. Finite element modeling of transverse impact on a ballistic fabric. *Int J Mech Sci* 2006;48:33–43.
- [11] Haseganu EM, Steigmann DJ. Analysis of partly wrinkled membranes by the method of dynamic relaxation. *Comput Mech* 1994;14:596–614.
- [12] Haseganu EM, Steigmann DJ. Theoretical flexural response of a pressurized cylindrical membrane. *Int J Solids Struct* 1994;31:27–50.
- [13] Haseganu EM, Steigmann DJ. Equilibrium analysis of finitely deformed elastic networks. *Comput Mech* 1996;17:359–73.
- [14] Kwong K, Goldsmith W. Lightweight ballistic protection of flight-critical components on commercial aircraft – ballistic characterization of zylon. FAA Report DOT/FAA/AR-04/45, P1; 2004.
- [15] Lim CT, Tan VBC, Cheong CH. Perforation of high-strength double-ply fabric system by varying shaped projectiles. *Int J Impact Eng* 2002;27:577–91.
- [16] Lim CT, Shim VPW, Ng YH. Finite-element modeling of the ballistic impact of fabric armor. *Int J Impact Eng* 2003;28:13–31.
- [17] Pangiotopoulos PD. A variational inequality approach to the inelastic stress-unilateral analysis of cable structures. *Comput Struct* 1976;6:133–9.
- [18] Papadrakakis M. A method for the automatic evaluation of the dynamic relaxation parameters. *Comput Meth Appl Mech Eng* 1980;25:35–48.
- [19] Phoenix SL, Porwal PK. A new membrane model for the ballistic impact response and V_{50} performance of multi-ply fibrous systems. *Int J Solids Struct* 2003;40(24):6723–65.
- [20] Pipkin AC. The relaxed energy density for isotropic elastic membranes. *IMA J Appl Math* 1986;36:297–308.
- [21] Powell D, Zohdi TI, Johnson G. Multi-scale modeling of structural fabric undergoing impact. FAA Report DOT/FAA/AR-08/38; 2008.
- [22] Shockey DA, Erlich DC, Simons JW. Lightweight ballistic protection of flight-critical components on commercial aircraft – large-scale ballistic impact tests and computational simulations. FAA Report DOT/FAA/AR-04/45, P2; 2004.
- [23] Steigmann DJ. Tension field theory. *Proc R Soc Lond A* 1990;429:141–73.
- [24] Tabiei A, Jiang Y. Woven fabric composite material model with material nonlinearity for finite element simulation. *Int J Solids Struct* 1999;36:2757–71.
- [25] Tan VBC, Shim VPW, Zeng X. Modelling crimp in woven fabrics subjected to ballistic impact. *Int J Impact Eng* 2005;32:561–74.
- [26] Toyobo. PBO fiber ZYLON. Report of the Toyobo Corporation, Ltd; 2001. Available from: www.toyobo.co.jp.
- [27] Verzemneiks J. Lightweight ballistic protection of flight-critical components on commercial aircraft – zylon yarn tests. FAA Report DOT/FAA/AR-05/45, P3; 2005.
- [28] Zohdi TI, Steigmann DJ. The toughening effect of microscopic filament misalignment on macroscopic fabric response. *Int J Fracture* 2002;115:L9–L14.
- [29] Zohdi TI. Modeling/simulation of progressive penetration of multilayered ballistic fabric shielding. *Comput Mech* 2002;29:61–7.
- [30] Zohdi TI, Powell D. Multiscale construction and large-scale simulation of structural fabric undergoing ballistic impact. *Comput Meth Appl Mech Eng* 2006;195:94–109.